Nuclear Science and Techniques (2023) 34:1
https://doi.org/10.1007/s41365-022-01161-4

Large area ^{3}He tube array detector with modular design for multi-physics instrument at CSNS

Lin Zhu[1,2,3] · Jian-Rong Zhou[1,2,3] · Yuan-Guang Xia[1,2] · Liang Xiao[1,2] · Hong Luo[1,2] · Xiao-Juan Zhou[1,2] · Wen-Qin Yang[1,2,3] · Bei-Ju Guan[1,2] · Xing-Fen Jiang[1,2] · Yan-Feng Wang[1,2] · Hong Xu[2] · Hai-Yun Teng[2] · Li-Xin Zeng[2] · Jia-Jie Li[2] · Lei Hu[2] · Ke Zhou[2] · Yong-Xiang Qiu[2] · Pei-Xun Shen[2] · Jun Xu[2] · Li-Jiang Liao[2] · Xiao-Zhuang Wang[2] · Gui-An Yang[1,2] · Huai-Chan Chen[2] · Ju-Ping Xu[2] · Zhi-Duo Li[2] · Song-Lin Wang[2] · Jian Zhuang[2] · Yu-Bin Zhao[1,2,3] · Jun-Rong Zhang[2] · Wen Yin[2] · Zhi-Jia Sun[1,2,3] · Yuan-Bo Chen[1,2]

Received: 5 July 2022 / Revised: 24 October 2022 / Accepted: 22 November 2022 / Published online: 6 January 2023

Abstract
The multi-physics instrument (MPI) is the first user cooperative instrument at the China Spallation Neutron Source (CSNS). It was designed to explore the structures of complex materials at multiple scales based on the neutron total scattering technique. This imposes the requirements for the detector, including a high detection efficiency to reduce the measurement time and a large solid angle coverage to cover a wide range of momentum transfers. To satisfy these demands, a large-area array of ^{3}He-filled linear position-sensitive detectors (LPSDs) was constructed, each with a diameter of 1 inch and pressure of 20 atm. It uses an orbicular layout of the detector and an eight-pack module design for the arrangement of ^{3}He LPSDs, covering a range of scattering angles from 3° to 170° with a total detector area of approximately 7 m^2. The detector works in air, which is separated from the vacuum environment to facilitate installation and maintenance. The characteristics of the MPI detector were investigated through Monte Carlo (MC) simulations using Geant4 and experimental measurements. The results suggest that the detectors are highly efficient in the wavelength range of the MPI, and an efficiency over 25% is achievable for above 0.1 Å neutrons. A minimal position resolution of 6.4 mm full width at half maximum (FWHM) along the tube length was achieved at a working voltage of 2200 V, and a deviation below 2 mm between the real and measured positions was attained in the beam experiment. The detector module exhibited good consistency and an excellent counting rate capacity of up to 80 kHz, which satisfied the requirements of experiments with a high event rate. Observations of its operation over the past year have shown that the detector works steadily in sample experiments, which allows the MPI to serve the user program successfully.

Keywords Neutron detector · LPSD · Position resolution · Counting rate capacity

This work was supported by the National Key R&D Program of China (No. 2021YFA1600703), National Natural Science Foundation of China (No. 12175254), and Youth Innovation Promotion Association CAS.

✉ Jian-Rong Zhou
zhoujr@ihep.ac.cn

✉ Zhi-Jia Sun
sunzj@ihep.ac.cn

1 Institute of High Energy Physics, Chinese Academy of Sciences, Beijing 100049, China

2 Spallation Neutron Source Science Center, Dongguan 523803, China

3 University of Chinese Academy of Sciences, Beijing 100049, China

1 Introduction

As unique neutral particles different from X-rays, neutrons interact with materials via nuclear and magnetic interactions. This renders them suitable for high penetration through neutron scattering to examine matter in extreme environments with high temperatures, high pressures, and strong magnetic fields. Moreover, the wavelength of neutrons is close to the atomic spacing, and their thermal energy approaches the energy of elementary excitation in solids. This indicates that neutron scattering can be applied to research the structure and dynamics of materials. Over the past few decades, sustained and continual developments in experimental methods have significantly increased the sensitivity and range of applications of neutron scattering, which has led to more stringent demands on the quality of the neutron source beam and the resolution of the neutron instrument in terms of counting rate capacity. In recent decades, significant progress has been made in material and life sciences with the development of next-generation high-flux neutron facilities, including the Spallation Neutron Source (SNS) in the USA [1], ISIS Neutron and Muon Source (ISIS) in the UK [2], Japan Proton Accelerator Complex (J-PARC) in Japan [3], China Spallation Neutron Source (CSNS) in China [4], and European Spallation Source (ESS) in Europe [5]. The CSNS [6, 6] is a large scientific facility that houses a new-generation high-flux and pulsed neutron source, which is based on an intense pulsed proton beam bombarding a tungsten–tantalum (W-Ta) target to produce neutrons. In the first phase (CSNS-I), the construction of three-neutron scattering instruments, the small angle neutron scattering spectrometer (SANS) [8, 8], multi-purpose reflectometer (MR) [10] and general purpose powder diffractometer (GPPD) [11] was completed, with 17 beamlines [12–14] left to be designed and built. In early 2020, the CSNS achieved the first phase of stable operation at a power of 100 kW with a pulse repetition of 25 Hz. In the upgrading phase (CSNS-II) [15], the accelerator power will be increased to 500 kW.

The multi-physics instrument (MPI) [16, 16], the fourth neutron scattering instrument built at the CSNS, is the first neutron total scattering diffractometer in China and CSNS's first user-cooperative instrument. It was constructed as a collaborative project by the Dongguan University of Technology and the City University of Hong Kong. It is mainly used for research on materials with different ordered structures, focusing on the structural analysis of long-range order and locally disordered materials as well as long-range disorder and short-range ordered materials through the total scattering or pair distribution function (PDF) technique. Traditionally, neutron diffraction measurements have focused on accurate measurements of the positions and intensities of Bragg peaks. The former provide good determination of the lattice parameters, and the latter yield information about the average positions of the atoms. However, the PDF uses the entire diffraction pattern, Bragg and diffuse components, to describe the complete system information of the real structure, from long-range ordered down to localized imperfections. The MPI was designated as beamline-16 of the CSNS target station, and the neutron beam was extracted from a decoupled water moderator. A double T0 chopper is used to collect neutron data with a short wavelength while shielding the fast neutron and gamma flash yielded at the moment of the spallation reaction. Three disk choppers are installed downstream of the T0 chopper and form a T1 chopper and two T2 choppers to adjust the bandwidth of the wavelength flexibly and limit the range of the standard operating wavelength of the MPI to 0.1–3 Å.

The PDF theory requires a wide moment transfer (Q) range coverage to achieve a high real-space resolution and medium—high Q resolution to obtain the resolution of Bragg peaks, and Q is extracted from the spatial position and time-of-flight (TOF) of scattering neutrons. To satisfy these requirements, the MPI requires a detector with a wide coverage of the scattering angle near 180°, a spatial resolution of less than 10 mm along the tube direction, and high efficiency for short-wavelength neutrons (<1 Å). The helium-3 filled linear position sensitive detector (LPSD), a commercial product with mature technology, has been widely utilized and operated at existing neutron scattering facilities worldwide owing to its stability, ease of maintenance, large-area production, lower noise, excellent neutron/gamma discrimination, and good timing [18–21]. It was ultimately recognized as the practical detector choice and can attain a high detection efficiency by increasing the pressure of ^{3}He gas. The large-area array detector built at the MPI is based on a modular design and involves 576 ^{3}He LPSD tubes that are installed around the vacuum tank to cover an active area of 7 m^2 and a scattering angle from 3° to 170°. In the first phase of construction of the MPI, 240 ^{3}He tubes were manufactured by Reuter–Stokes and assembled into 30 modules to provide a range of scattering angles from 31° to 170° and a total area of detection of approximately 3 m^2. To facilitate the maintenance and operation of the detector, the array operates in an atmospheric environment that is separated from the sample environment. Moreover, a high counting rate capacity and wide dynamic range are indispensable. The former requires a small timing resolution and high-speed data transmission for the detector, whereas the latter adapts it to sample experiments with different scattering intensities.

2 Detector design

2.1 Principle and simulation of efficiency of ^{3}He LPSD

Thermal neutron detection by the ^{3}He LPSD relies on the following nuclear reaction:

$$n + {}^3\mathrm{He} \rightarrow p + T + E_Q = 764\,\mathrm{keV},$$
$$\sigma = 5315.77\ \mathrm{barn\ for}\ E_\mathrm{n} = 25.3\,\mathrm{meV}. \quad (1)$$

This indicates that a thermal neutron reacts with one ^{3}He nucleus to generate two daughter products: a proton and a tritium ion. The products of this reaction move in opposite directions from the reaction point and share a 764 keV reaction energy, of which the proton takes 573 keV and the tritium ion takes 191 keV. The ^{3}He LPSD was fabricated using thin-walled stainless steel, which acts as the detector cathode. A thin tensioning wire with uniform resistivity was installed along the length of the tube and serves as the anode of the detector. It is sensitive to its position along the anode wire. Compared with the multiwire proportional chamber (MWPC), the ^{3}He tube is superior in terms of facilitating large-area array fabrication and easy maintenance.

The capacity of location of the scattering neutron plays a critical role in the design of neutron scattering instruments. Based on the charge division principle, the ^{3}He LPSD can determine the location of a neutron hit along the direction of the anode wire, as shown in Fig. 1. Secondary charged particles from the neutron react with ^{3}He deposit energy, and ionize the working gas to create electron–ion pairs that are the primary signal of the detector. However, the signal was too weak to be recorded by the readout electronics. To improve the signal-to-noise ratio (SNR) of the neutron event, a gas multiplication effect was produced by creating a high electric field in the center of the LPSD tube and applying a high anode bias voltage at the anode. The neutron signal was amplified through the avalanche effect, which occurs in a region near the anode wire and produces a large charge cloud. Electrons in the charge cloud move toward the anode and quickly reach it, while ions with lower velocity travel to the cathode. This indicates that the latter makes a major contribution to the detector signal. The movement of the charge cloud creates a pulse current in the anode wire that is transmitted toward both ends of the tube. The current signals are collected and converted to voltage signals, the amplitudes of which represent the charge values of the neutron event.

A high detection efficiency is indispensable for sample experiments in neutron instruments. This not only reduces the measurement time but also improves the utilization ratio of the neutron beam. The MPI demands an operating wavelength range of 0.1–3 Å, which covers the range of energy from thermal neutrons to epithermal neutrons. To evaluate the efficiency of the ^{3}He LPSD, Monte Carlo (MC) simulations were performed in Geant4 [22]. A detector with a 500-mm-long rectangular prism with depth of 19.95 mm (the average depth of gas in a ^{3}He tube) was built in the Geant4 program and filled with ^{3}He gas. Four pressure values of ^{3}He gas were used in this case, and the sources of the neutrons with different wavelengths were set to irradiate the detector. Figure 1b shows the average distribution of ^{3}He tubes filled with different pressures. The detector filled with ^{3}He gas at a pressure of 20 atm yielded

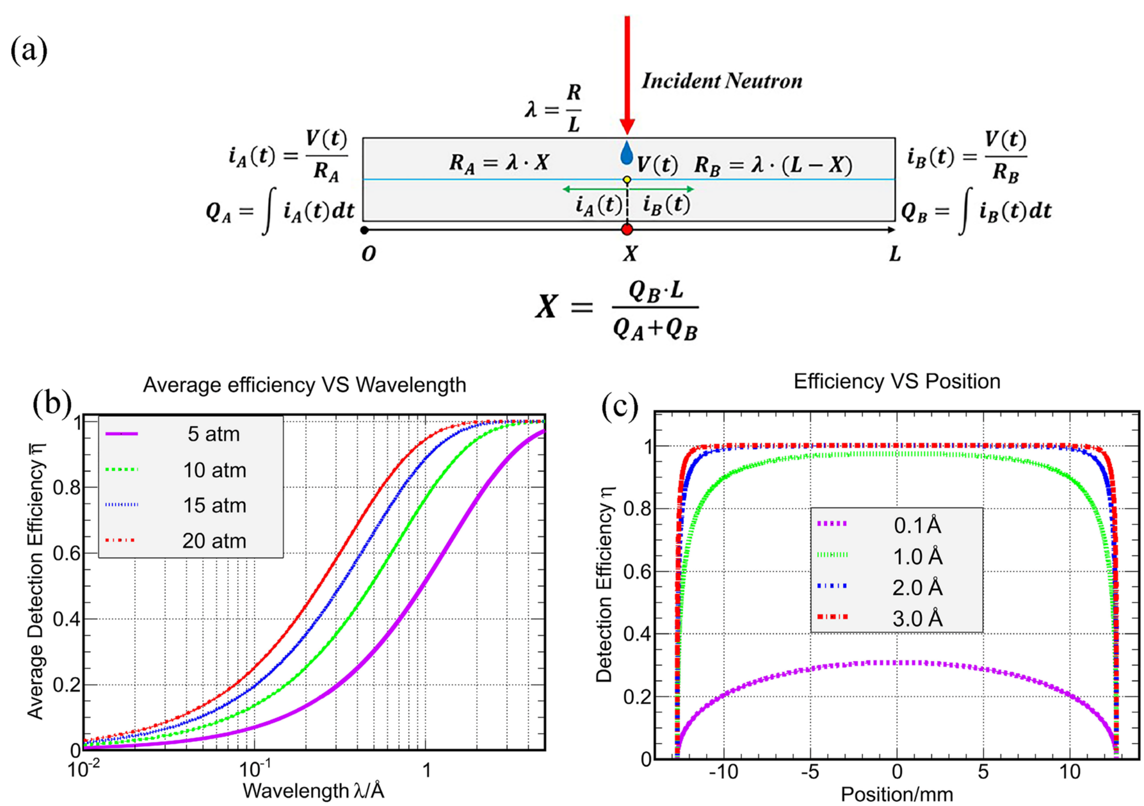

Fig. 1 **a** Schematic of the charge division of the ^{3}He linear position-sensitive detector (LPSD) tube, **b** average detection efficiency of 1-inch ^{3}He LPSDs filled with different pressures, **c** positional response of the efficiency of detection of neutrons with different wavelengths of the 1-inch ^{3}He LPSD with a pressure of 20 atm

an average efficiency of above 25% for 0.1 Å neutrons and almost 100% for 2 Å neutrons. An increase in the pressure of the ^{3}He gas improved the detection efficiency of the detector, and ^{3}He gas at a higher pressure required a higher bias voltage for the anode. For safety, the ^{3}He LPSD with a pressure of 20 atm was considered suitable for satisfying the efficiency requirements of the MPI.

Meanwhile, the incident direction and energy of the neutron significantly affect the detection efficiency. Therefore, a 1-inch, 500-mm-long tube model was constructed and filled with ^{3}He gas at a pressure of 20 atm, and four neutron sources with four wavelengths were used to illuminate the tube along the direction vertical to its diameter. As shown in Fig. 1c, "Position" represents the distance between the cross point of the diameter and the incident direction to the anode. The efficiency sharply declined near the region of the ends of the diameter owing to a decrease in the effective depth of the gas in the detector and the effects of the wall. For neutrons with wavelengths greater than 1 Å, a rectangular efficiency distribution was observed, which diminished the impact of the incident direction of the neutrons. Therefore, the 20 atm ^{3}He LPSD was adequate for use within the operational wavelength of the MPI.

2.2 Structure of the detector

Air significantly influenced the measurement results of the neutron scattering experiments. Thus, we designed a large evacuated tank with a vacuum environment in the MPI to reduce the influence of air scattering. It had a volume of 12 m^3, which was sufficient for installing devices to create an extreme environment for the sample to satisfy specific experimental demands and could be operated at a pressure ranging from 100 to 1×10^{-6} mbar during the experiment. To facilitate operation and maintenance, the detector was designed to operate under atmospheric conditions isolated from the sample environment. As shown in Fig. 2a, the detector was based on a modular design consisting of 13 banks (Bank01 to Bank13), which were symmetrical with respect to the beam path, and eight ^{3}He LPSDs fixed on a module as a detector unit mounted on these banks. The main body of the bank was made of nonmagnetic stainless steel, which resulted in long-term stability without mechanical

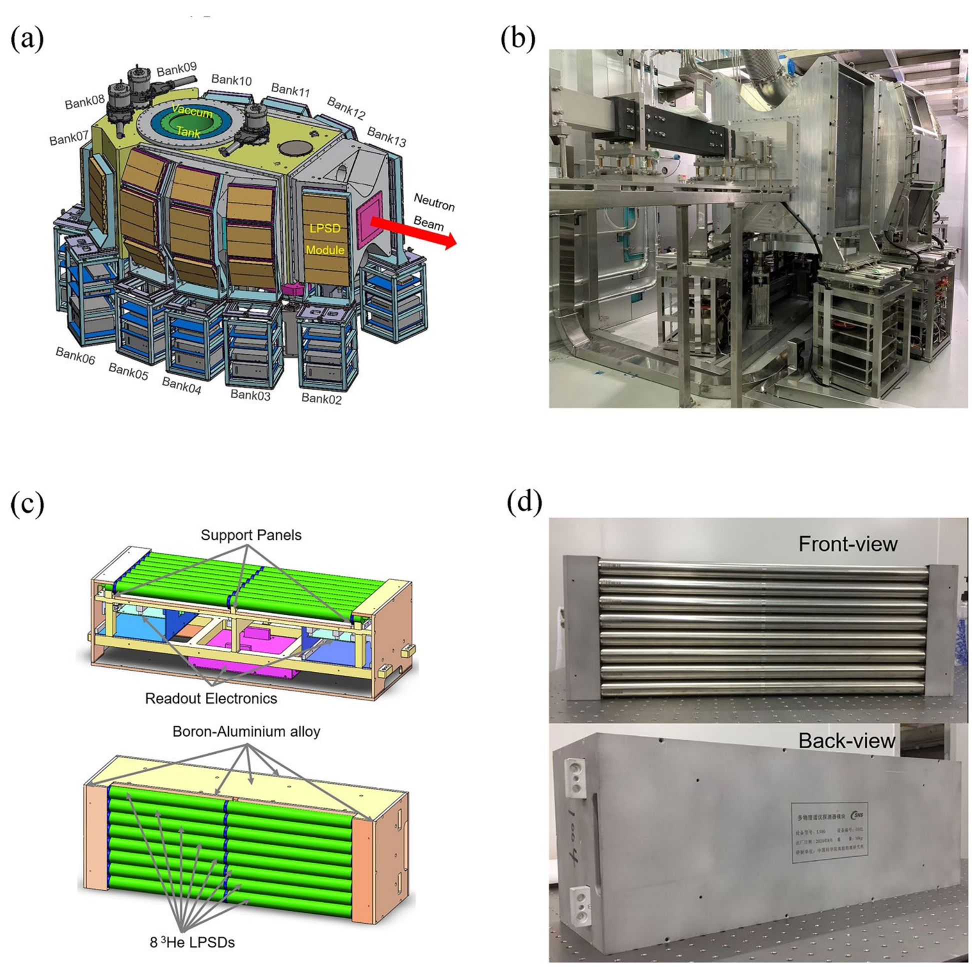

Fig. 2 **a** Layout and **b** site photograph of the multi-physics instrument (MPI) detector; **c** computer model and **d** physical photograph of a 500 mm LPSD module assembled

deformation and satisfied the special requirements of the sample environment. These banks were divided into two types: those with a single-plane support structure and those with a three-plane support structure to match the shape of the scattering chamber. An adjusting system was fixed at the bottom of each bank to provide a convenient means of altering its position during installation. Figure 2b shows a photograph of the detector array installed in the MPI scattering room. The unfilled regions in the banks were reserved for the detector modules that were built in the second phase of the MPI, and B_4C plastic plates were fixed at it to absorb the stray neutrons and reduce the level of neutron background in the scattering room during operation.

The complete MPI detector contains 576 ^{3}He LPSD tubes, which are arranged into 72 modules to cover an active area of approximately 7 m^2 with a scattering angle ranging from 3° to 170°. For the Phase-I construction of the MPI, 240 ^{3}He tubes were manufactured by Reuter–Stokes. Two specifications of LPSDs with active lengths of 300 and 500 mm were used to satisfy the demands of the MPI. The latter LPSDs are considered in detail in this paper. These LPSD tubes formed a large-area detector array of 30 modules covering an active area of 3 m^2 and scattering angles ranging from 31° to 170°. The detector modules were fixed at Bank03 to Bank12, and all modules in a bank covered a close scattering angle. Bank07 and Bank08 contained four detector modules with an active length of the ^{3}He tube of 300 mm, and were completed during this construction. The detector modules with 500 mm active length ^{3}He tubes were installed at the other banks. Figure 2c presents the computer model of the LPSD module with an active length of 500 mm, which shows the outer shape of the detector module. Only the detector plane, which formed the active area of the module and comprised eight ^{3}He tubes, was exposed to capture the neutrons scattered by the sample. The ^{3}He tubes were mounted onto three support panels shaped as semicircular grooves to support the tube. The coaxial tolerance of each set of grooves needed to be below 0.1 mm to guarantee the straightness of the ^{3}He tube. Near every support point there was a 5-mm-wide and 0.1-mm-thick stainless steel strip to fix the tube tightly to the support. A simple frame structure made of high-strength aluminum alloy was used inside the detector module. It reduced the overall weight and facilitated cooling of the electronic system by air, while guaranteeing the reliability of the repetitive assembly. The front-end electronics boards were installed under the ^{3}He tube to achieve good grounding performance and reduce the stray capacitance, whereas the digital electronics were located close to the front-end boards to reduce electromagnetic interference. In addition, the lateral and back plates utilized a 5-mm-thick boron–aluminum alloy that provided effective radiation shielding for the readout electronic system inside the module. At the same time, it served as an electromagnetic shield for the entire detector unit to isolate it from outer interference, thus creating an ideal condition for the stable operation of the detector module. Figure 2d shows a 500 mm LPSD module assembled in the laboratory. A customized logo can be observed in the back plate, which provides the serial number and module type of this detector module.

3 Readout electronics and DAQ system

With the increase in the neutron flux applied to neutron diffraction, the consequent high data rates are challenging for the readout electronics in terms of signal processing and the DAQ system in terms of data transmission. Similar to the detector module, the readout electronics were modularized and installed inside the detector module to form an entire unit. Each module contained independent readout electronics composed of two front-end boards and a digital readout board [23], as depicted in Fig. 3. The ^{3}He tubes fixed in a

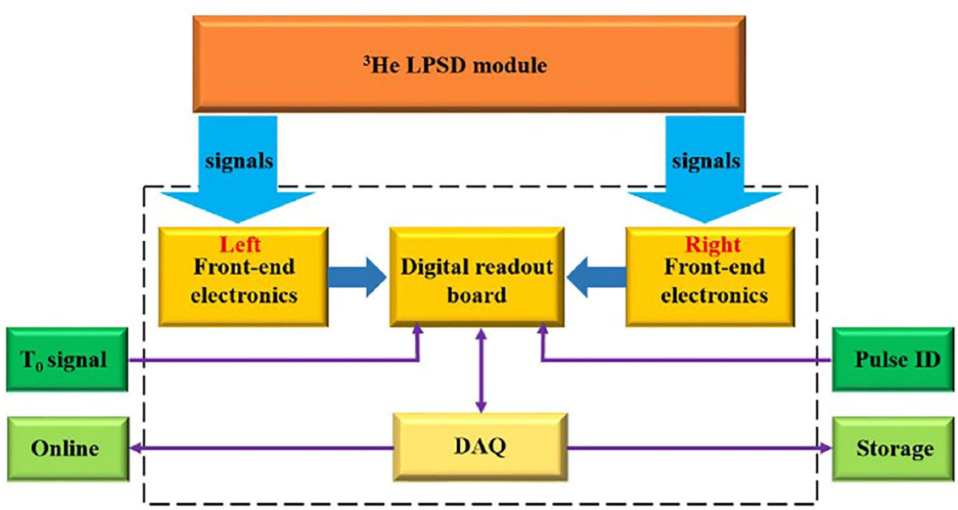

Fig. 3 Structure diagram of readout electronics and DAQ

module shared one channel bias voltage, which simplified the HV supply device. The front-end electronics consisted of eight-channel analog circuits that were mutually independent, and each channel had a charge-sensitive preamplifier and shaper along with a direct connection to the ^{3}He LPSD. A test circuit was retained, which was beneficial for debugging and performance during testing. The digital electronics were based on field-programmable gate array (FPGA) technology and had 16 analog-to-digital converters (ADC) that matched with the front-end board's output channels. A firmware program was configured in the FPGA to calculate the relevant information of the incident neutron. An external triggering signal of 25 Hz is provided by the CSNS accelerator system, and this serves as the starting time, that is, T0, for the travel of the neutrons. The time-stamp Pulse ID was used to mark every T0 signal. Once a neutron incident on the detector was captured, the front-end electronics collected the signals from both ends and amplified, filtered, and shaped them. The processed signals were then fed into the digital board for further processing to obtain information about the hit position and TOF.

The DAQ is based on the Linux operating system and was developed using C++. There are two optical modes set in the DAQ: a noise test mode to examine the detector system and a run control mode for instrument operation. The DAQ interacts with the readout electronics through high-speed fibers to implement the parameter configuration for electronic and neutron data collection. It is configurable for online data visualization and local data storage, which is significant for device operation monitoring and debugging as well as for further detailed data analysis. Moreover, a large amount of data is created in the detector system during the instrument operation, which needs to be collected and transmitted to the local servers in real time to avoid data loss. The DAQ reserves a sufficiently large bandwidth for each ^{3}He detector module in the detector array for data transmission. This satisfies the data readout under an event rate of 14.4 MHz for all detector modules built into the MPI.

4 Performance of the detector

A series of neutron beam experiments, including module calibration, position resolution, timing resolution, and counting rate capacity measurements, were conducted to investigate and evaluate the performance of the ^{3}He LPSD module.

4.1 Position calibration

In a neutron scattering instrument, a detector with a high spatial resolution and positioning accuracy is required to record the spatial distribution of neutrons scattered by the sample. For ^{3}He LPSDs, it is imperative to determine the relationship between the actual position of irradiation in the tube direction and the position measured by the detector. Experimentally, it is given by the formula Real_Position = Slope × Measured_Position + Intercept, where the Slope and Intercept represent the correction factors in the linear relation provided by the position calibration experiment. The peak position in the raw count distribution of each irradiated point along the tube path is the Measured_Position item, whereas the Real_Position item represents the actual position of each site. Figure 4a shows a schematic of the module calibration. A 3-mm-thick mask with seven slits, each with a width of 1 mm, made of boron-aluminum alloy, was mounted close in front of the detector module. A polyethylene brick was placed at the beam exit, which scattered the neutron beam to cover the active detection area of the module. Thus, the eight ^{3}He LPSDs in the module can be calibrated simultaneously. Figure 4b shows a site photograph of the position calibration. The center of the detector module was aligned to the neutron beam by a laser aligner (as seen in the inset), and two boron-aluminum alloy plates were placed separately at the bottom and top of the module to offer adequate shielding for the marginal ^{3}He tubes on the module. Ideally, the module should be illuminated by a uniform neutron beam. In this example, polyethylene bricks with different thicknesses were tested, and the 30-mm-thick one was the optimal solution. The actual positions of the slits in the mask used here were 25.6, 100.6, 175.6, 250.6, 325.6, 400.6, and 475.6 mm, respectively. This constituted an array of seven numbers representing the real positions of the slits for the following calibration.

The calibration experiment was performed at HV = 2200 V. The raw positions measured by each ^{3}He LPSD were extracted from the Gaussian function fitting to every peak in the raw count distribution along the tube path, which formed a one-dimensional array with seven numbers. The linear function mentioned above was then used to fit the two arrays to obtain the correction coefficients. Figure 4c shows the calibration curve fitted by the linear function for a ^{3}He LPSD in the module, and the results of the fitting are provided in the legend. It reveals that the correction coefficients Slope = 1.415 and Intercept = − 102.1 are used for the position reconstruction of this ^{3}He tube, while the "Prob" is almost equal to one, which signifies a good position correlation for this calibration curve. After completing the position calibration for every ^{3}He LPSD in the detector module, the actual count distribution of each tube was reconstructed. As shown in Fig. 4d, there are seven straight slits in the 2D count distribution of the module, where the positions of these slits are consistent with their actual positions. However, slight distortions appear in the image of the two slits near the tube's ends, which result from the decline of the

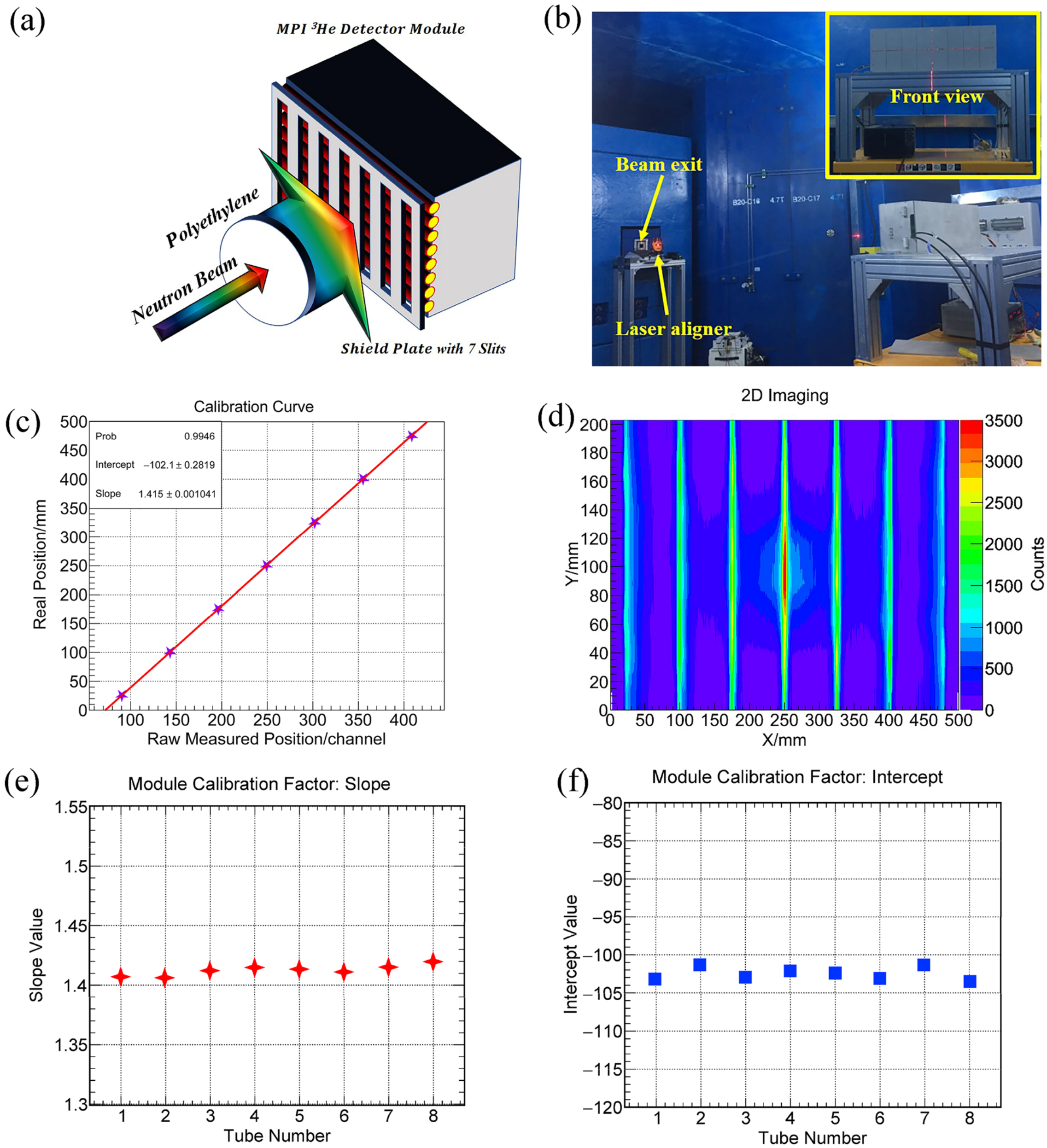

Fig. 4 **a** Schematic drawing and **b** site photograph of ^{3}He LPSD's positioncalibration, **c** calibration curve of a single ^{3}He LPSD in a module, **d** corrected distribution of module counts, **e** slope values, and **f** Intercept value in a module

position resolution of the ^{3}He tube at those sites, which will be discussed in the next section. The distributions of the calibration coefficients for the eight ^{3}He tubes in a module are displayed in Fig. 4e, f, which clearly show that the calibration factors of the tubes in this module exhibit good consistency. The values of slope are all nearly equal to 1.41 while those of intercept are equal to – 102. The excellent consistency of the calibration coefficients also reflects the good performance of the ^{3}He LPSD tubes in the detector module.

4.2 Position resolution

Neutron scattering experiments using the PDF method require high-precision measurements for momentum transfer (Q). Thus, the detector must not only have a high spatial resolution but also ensure sufficiently high positional accuracy. A spatial resolution of 10 mm is stipulated in the MPI design and is defined as the full width at half maximum (FWHM) of the position distribution along the tube path. The experimental setup was similar to that shown in Fig. 4b, except that the mask was replaced with a single slit, and a lead brick with thickness of 10 cm was placed at the exit of the beam to reduce the neutron flux. The tests for the position resolution were carried out through the irradiation of different sites of the detector by neutrons, and the hit positions of neutrons along the tube direction were corrected by the factors considered in Sect. 4.1. Figure 5a presents the count distribution of a single ^{3}He LPSD and the results of the fitting using the Gaussian function (working HV = 2200 V). The spatial resolution was calculated using the formula FWHM = 2.355 × sigma. The best resolution (6.4 mm) was located at the center site along the tube length. As depicted in Fig. 5b, there was excellent position linearity in the ^{3}He LPSD. This indicates that a deviation of less than 2 mm between the real and measured positions is attainable. To find a suitable working HV for instrument operation in future, three HV values were used in this test. Figure 5c shows the distribution of the FWHM of the ^{3}He tube in the module at different working HVs. It indicates that an HV value greater than 2150 V is adequate for the implementation of a position resolution below 10 mm, and a better resolution can be realized using a higher working HV. Further, it is noteworthy that there is a concave shape that the FWHM gradually decreases along directions to both ends of the ^{3}He tube, and the best one is situated in the center point. This is mainly derived from the charge-equalization effect [24], which is caused by the front-end board in the readout electronics system. The charge-equalization effect arises from the difference between the input impedance and the ideal impedance (as depicted in Fig. 1a), which yields additional noise to the front-end board, leading to inaccurate

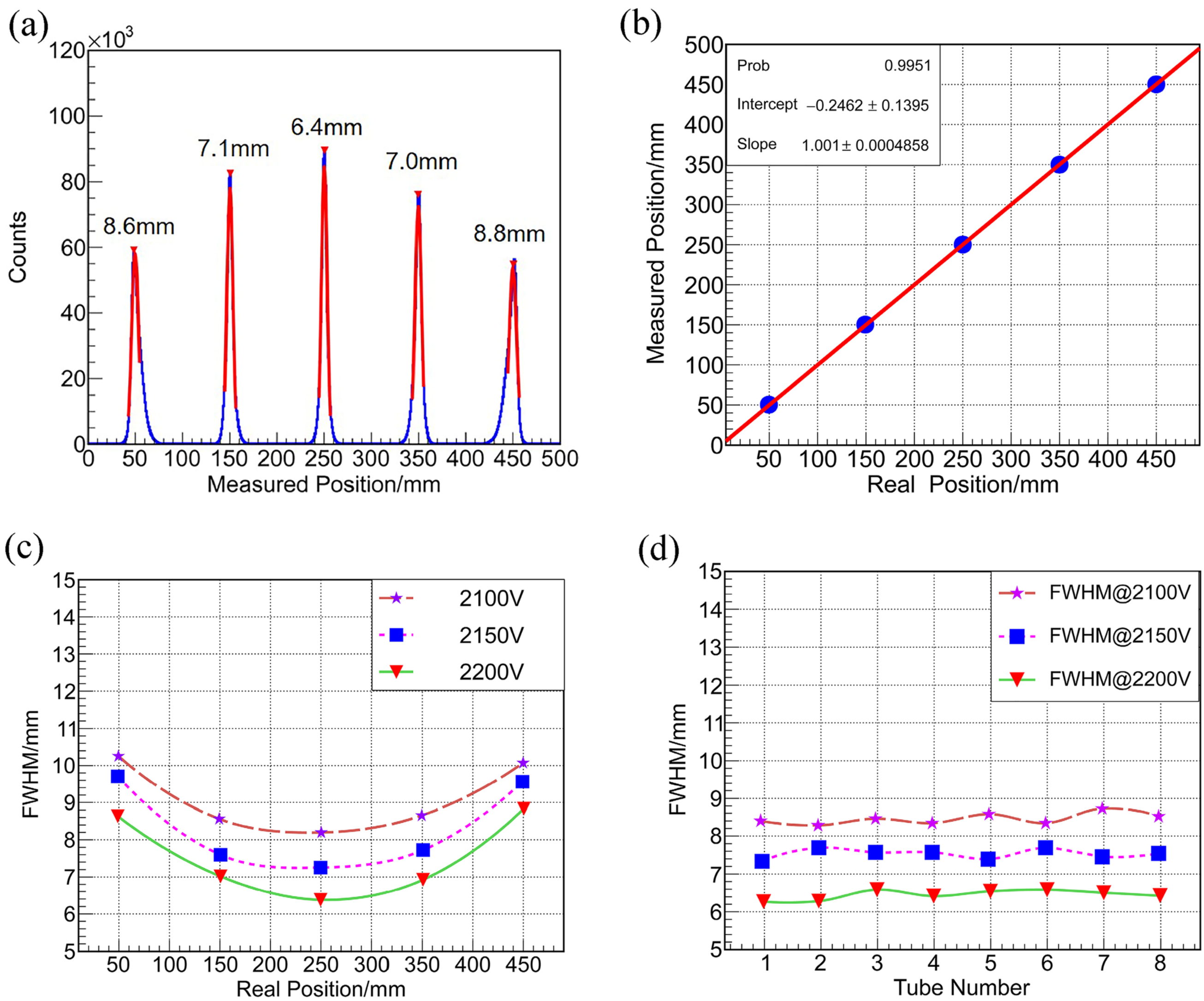

Fig. 5 **a** Count distribution of a ^{3}He tube in the module and its full width at half maximum (FWHM) fitted by the Gaussian function, **b** position-linearity of a ^{3}He tube in the module, **c** variations in the FWHM of the irradiated sites at three HV values, **d** FWHMs in a module for the three HV values

position measurement. Figure 5d depicts the spatial resolution distribution of ^{3}He LPSDs in the detector module at the 250 mm position, and it shows good agreement in terms of the position resolutions of the module. The fluctuation in the FWHM in the module stems from the difference in the ^{3}He tube, and the average of the minimal resolutions in the module can reach less than 9 mm. Considering the application requests of MPI and the safe operation of the detector array, a value of 2150 V for the HV will be applied in the experiments on the sample under normal operation.

4.3 Timing resolution

The maximum counting rate of the ^{3}He LPSD is primarily confined to the timing resolution, which is defined as the minimum interval at which the detector can distinguish events generated by two successive incoming neutrons. It depends on the signal width created in the detector and the intrinsic time resolution of the readout electronics. To measure the timing resolution of the ^{3}He LPSD, the direct neutron beam was used to irradiate the detector and the electronic system recorded the TOF distribution of the incident neutrons. As shown in Fig. 6a a serious deformation in the TOF spectrum occurs because of the accumulation of signals in the readout electronics. A 4.2 μs timing resolution of this detector can be obtained from Fig. 6b, which verifies the good timing resolution of the MPI detector array.

4.4 Counting rate capacity

Counting rate capacity is an important representation for the evaluation of neutron diffraction instruments. Specifically, it primarily influences the positioning accuracy under a high-flux situation and the count loss under a high scattering intensity status.

To investigate the influence of the counting rate on the position resolution, an experiment was conducted at beamline-20 of the CSNS, in the same way as reported in Sect. 4.2. However, the slit was aligned at the 250 mm position of the ^{3}He tube. Moreover, there was a non-uniform distribution of the neutron beam during the period of the pulse; therefore, a simple method was used to obtain the count distributions at different counting rates by extracting positional information at different intervals in the TOF. To avoid severe saturation of the ^{3}He tube, a lead block with a thickness of 5 cm was used and set at the beam exit. The measurement results are presented in Fig. 7a. A spatial resolution of less than 10 mm can be attained at an instantaneous counting rate of less than 10 kHz. A high instantaneous counting rate, especially over 10 kHz, leads to a deterioration of the spatial resolution. This decline caused by the high-flux beam mainly stems from two aspects: the space-charge effect [25] in the detector and pile-up of the pulse signal in the readout electronics. The main contribution of the movement of the charged ions, whose velocity limits the width of the signals in time, to signals in the ^{3}He tube easily leads to pulse pile-up in the front-end electronics. When irradiating a site along the tube path with a high-flux neutron, ions with a slow drift speed form an access electric field to weaken the original electric field intensity in the region near the anode. This directly degrades the detector gain. However, the signal pile-up will give rise to an inaccurate measurement of the magnitude of charge, which in turn deteriorates the accuracy of positioning. Figure 7b shows a simple schematic of the signal pile-up on the front-end board. It is clear that the amplitude of the pile-up signal is not normal and leads

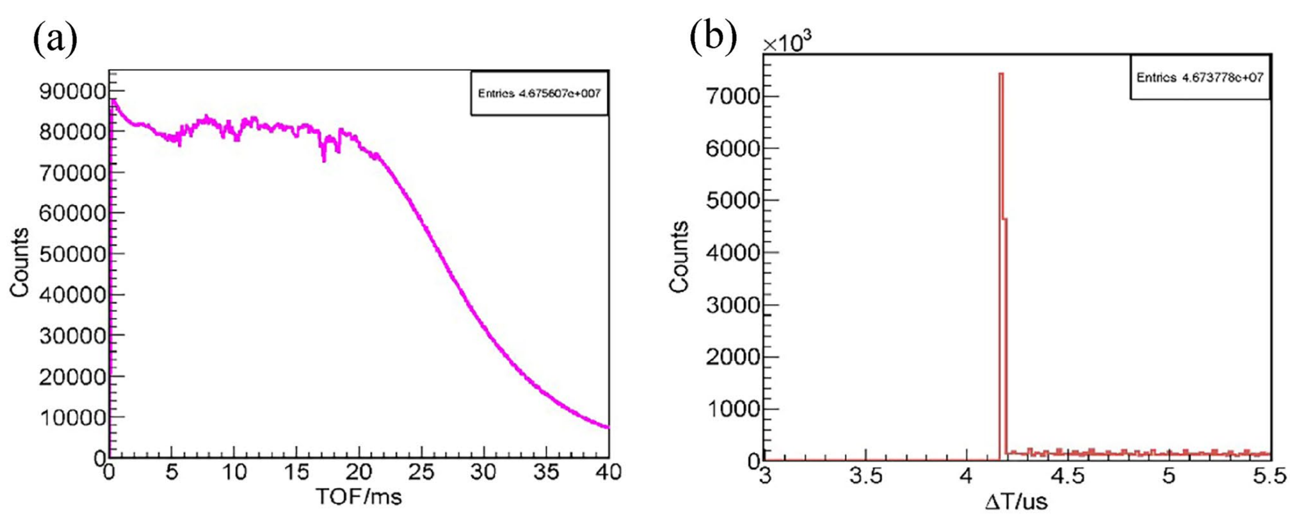

Fig. 6 **a** Time-of-flight (TOF) spectra of neutron recorded by the ^{3}He LPSD, and **b** time-interval distribution of the two neutron events

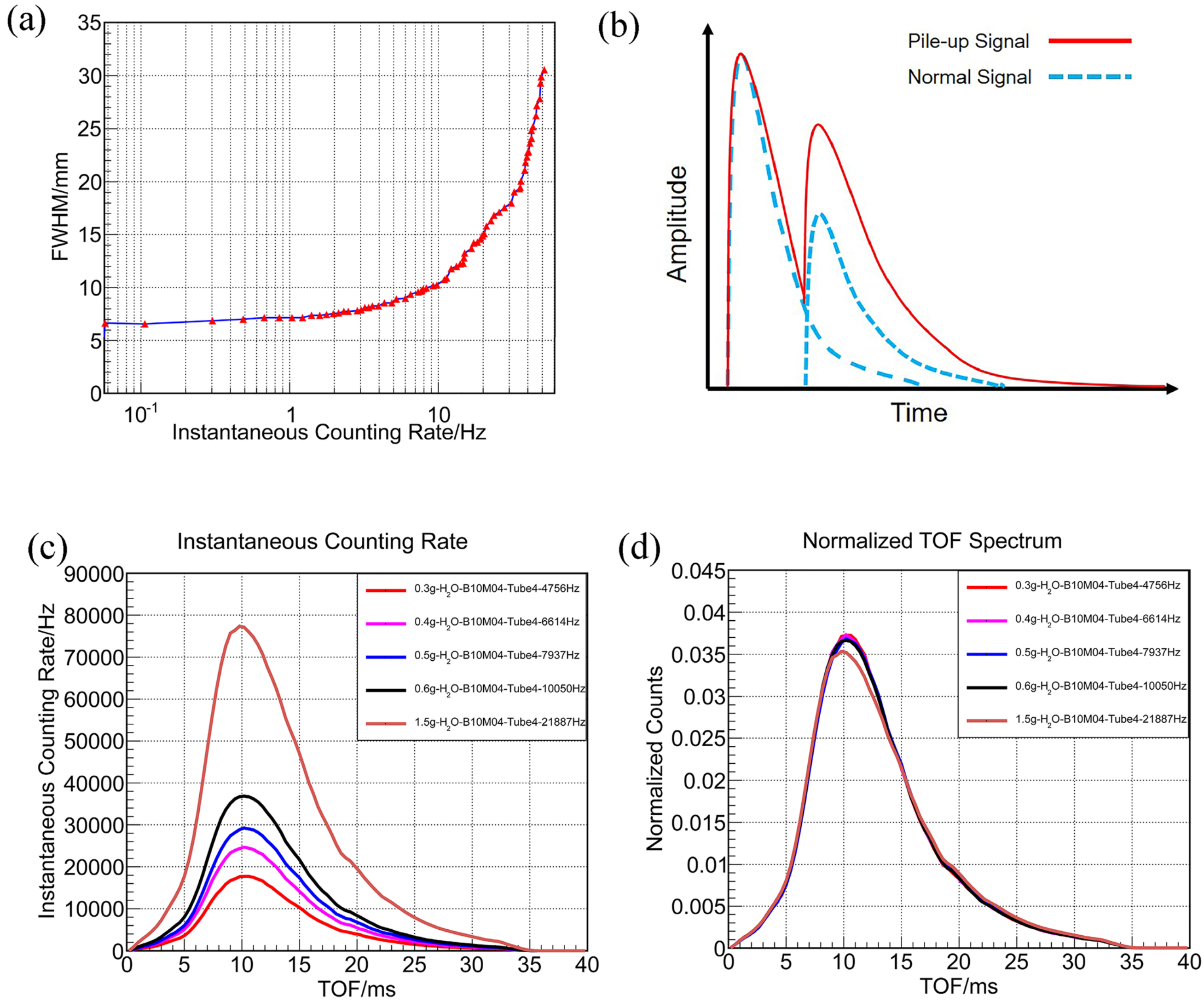

Fig.7 **a** Variations in FWHM with the counting rate, **b** the schematic drawing of signal pile-up, **c** the instantaneous counting rate distributions and **d** their normalized TOF spectra

to inaccurate position calculations, as shown in Fig. 1a. In some serious cases, a large signal with an amplitude over the normal working range of the readout electronics is formed, which leads to nonlinear saturation of the electronic system and increases the dead-time of the entire detector system.

The experimental efficiency was determined by the counting rate capacity in neutron scattering measurements. In an instrument the detector system of which is composed of a large-area detector array, the counting rate capacity is basically dependent on the detector system. In this study, a novel method was adopted to determine the influence of the counting-rate capacity of the detector. This experiment was conducted at the MPI beamline, and water samples of different masses were used to change the level of neutron flux irradiating the detector modules. Figure 7c displays the distributions of the instantaneous counting rates of the five water samples, and Fig. 7d shows the TOF spectra normalized by their total counts. The shapes of the TOF distributions of the different samples are essentially in agreement with one another. The peaks of the first four samples are located at 10.2 ms, whereas that of the last one is at 9.8 ms. The ratio of the instantaneous counting rate to the average one in the ^{3}He tube here is approximately equal to 3.6 and originates from the wavelength's maldistribution of the neutron beam in the MPI beamline. Additionally, the nonlinear saturation of the detector occurs in the TOF range from 9 to 13 ms for the 1.5 g water sample. The maximum average counting rate without the saturation effect of the ^{3}He tube is approximately 8 kHz, and the normalized value decreases with increasing sample mass. The minimum average count rate was 10 kHz when the detector was saturated. It is inevitable that event loss will exist in high-level counting rate experiments owing to the space charge effect in the detector and the pulse signal pile-up in the electronics. As discussed above, the signal pile-up causes count loss of the detector, which leads to a decline in the detection efficiency and distortion of the count distribution. In more severe cases (as discussed in Sect. 4.3), the TOF distribution is badly distorted, and the position resolution degenerates. This has a negative impact on the instrument operation and experimental results. Hence, the maximum average counting rate of up to 80 kHz is realizable and acceptable for the detector module of the MPI, whereas the total counting rate capacity of the entire detector array built in Phase I of the MPI is 2.4 MHz. From the above discussion of the spatial resolution, it can be concluded that the count loss in this measurement mainly occurred owing to the contribution of the pulse pile-up because of the high event rate distributed along the entire ^{3}He tube, and not just at one position. Therefore, the position resolution remained at a normal value and remained almost unaffected.

5 Summary and future work

In the MPI, 576 ^{3}He LPSD tubes were used to construct an array detector with an effective area of 7 m^2, covering a scattering angle ranging from 3° to 170°. It consists of 72 detector modules, each containing a set of independent readout electronics and eight ^{3}He tubes mounted on it. The total event rate capacity of 14.4 MHz is reachable by the DAQ for the entire detector array. In the first phase of MPI construction, 240 ^{3}He LPSD tubes with active lengths of 300 and 500 mm were used. A construction project in which the sample is placed in a vacuum environment while the detector works in atmospheric conditions was adopted, which facilitates the on-site maintenance of the detector. With a detection efficiency of over 25% for more than 0.1 Å neutrons, an optical position resolution of 6.4 mm, excellent position linearity, and a high counting rate capacity of up to 80 kHz for the detector module, the MPI detector has been operating successfully in the user program for nearly one year and has yielded a large amount of data with high statistical accuracy for users to explore the inner structure of the material. To ensure that the instrument satisfies the application requirements of the high-flux status in the CSNS-II phase and continue producing world-level science, a detector with all the modules should be constructed and the corresponding electronics system should be updated to allow it to keep supporting the scientific community for many years to come.

Authors' contribution All authors contributed to the study conception and design. Material preparation, data collection and analysis were performed by Lin Zhu, Jian-Rong Zhou, Yuan-Guang Xia, Liang Xiao, Hong Luo, Xiao-Juan Zhou, Wen-Qin Yang, Bei-Ju Guan, Xing-Fen Jiang, Yan-Feng Wang, Hong Xu, Hai-Yun Teng, Li-Xin Zeng, Jia-Jie Li, Lei Hu, Ke Zhou, Yong-Xiang Qiu, Pei-Xun Shen, Jun Xu, Li-Jiang Liao, Xiao-Zhuang Wang, Gui-An Yang, Huai-Chan Chen, Ju-Ping Xu, Zhi-Duo Li, Song-Lin Wang. The first draft of the manuscript was written by Lin Zhu and all authors commented on previous versions of the manuscript. All authors read and approved the final manuscript.

References

1. T.E. Mason, D. Abernathy, I. Anderson et al., The Spallation Neutron Source in Oak Ridge: A powerful tool for materials research. Physica. B **385–386**, 955–960 (2006). https://doi.org/10.1016/j.physb.2006.05.281
2. J.W. Thomason, The ISIS spallation neutron and muon source—The first thirty-three years. Nucl. Instrum. Meth. A **917**, 61–67 (2019). https://doi.org/10.1016/j.nima.2018.11.129
3. Y. Oyama, J-PARC and new era of science. Nucl. Instrum. Meth. A **562**, 548–552 (2006). https://doi.org/10.1016/j.nima.2006.02.139
4. H.S. Chen, X.L. Wang, China's first pulsed neutron source. Nat. Mater **15**, 689–691 (2016). https://doi.org/10.1038/nmat4655
5. M. Lindroos, S. Bousson, R. Calaga et al., The European Spallation Source. Nucl. Instrum. Meth. B **269**, 3258–3260 (2011). https://doi.org/10.1016/j.nimb.2011.04.012
6. T.Y. Tang, Q. An, J.B. Bai et al., Back-n white neutron source at CSNS and its applications. Nucl. Sci. Tech. **32**, 11 (2021). https://doi.org/10.1007/s41365-021-00846-6
7. X.R. Xu, G.T. Fan, W. Jiang et al., Measurements of the ^{197}Au(n, γ) cross section up to 100 keV at the CSNS Back-n facility. Nucl. Sci. Tech. **32**, 101 (2021). https://doi.org/10.1007/s41365-021-00931-w
8. Y.B. Ke, C.Y. He, H.B. Zheng et al., The time-of-flight Small-Angle Neutron Spectrometer at China Spallation Neutron Source. Neutron News **29**, 14–17 (2018). https://doi.org/10.1080/10448632.2018.1514197
9. X.F. Jiang, J.R. Zhou, H. Luo et al., A large area ^{3}He tube array detector with vacuum operation capacity for the SANS instrument at the CSNS. Nucl. Sci. Tech. **33**, 89 (2022). https://doi.org/10.1007/s41365-022-01067-1
10. T. Zhu, X.Z. Zhan, S.W. Xiao et al., MR: The multipurpose reflectometer at CSNS. Neutron News **29**, 11–13 (2018). https://doi.org/10.1080/10448632.2018.1514196
11. J. Chen, L. Kang, H.L. Lu, The general purpose powder diffractometer at CSNS. Physica. B **551**, 370–372 (2018). https://doi.org/10.1016/j.physb.2017.11.005
12. A. Salman, J.R. Zhou, J.Q. Yang et al., First neutron Bragg-edge imaging experimental results at CSNS. Chin. Phys. Lett. **33**, 062901 (2022). https://doi.org/10.1088/0256-307X/39/6/062901
13. J. Chen, Z.J. Tan, W.Q. Liu et al., First neutron Bragg-edge imaging experimental results at CSNS*. Chin. Phys. B **30**, 9 (2021). https://doi.org/10.1088/1674-1056/ac0da7
14. J.P. Zhang, C.Y. Huang, Z.C. Qin et al., In-situ optical pumping for polarizing He-3 neutron spin filters at the China spallation neutron source. Sci. China Phys. Mech. Astron. **65**, 241011 (2022). https://doi.org/10.1007/s11433-021-1876-0
15. B. Wu, X. Li, Z. Li et al., Development of a large nanocrystalline soft magnetic alloy core with high mu 'pQf products for CSNS-II. Nucl. Sci. Tech. **33**, 99 (2022). https://doi.org/10.1007/s41365-022-01087-x
16. T.R. Liang, F. Shen, W. Yin et al., Monte Carlo shielding evaluation of a CSNS multi-physics instrument. Nucl. Eng. Technol. **51**, 1998–2004 (2019). https://doi.org/10.1016/j.net.2019.06.006

17. J.P. Xu, Y.G. Xia, Z.D. Li et al., Multi-physics instrument: total scattering neutron time-of-flight diffractometer at China spallation neutron source. Nucl. Instrum. Meth. A **1013**, 165642 (2021). https://doi.org/10.1016/j.nima.2021.165642
18. R.I. Bewley, J.W. Taylor, S.M. Bennington, LET, a cold neutron multi-disk chopper spectrometer at ISIS. Nucl. Instrum. Meth. A **637**, 128–134 (2011). https://doi.org/10.1016/j.nima.2011.01.173
19. J.K. Zhao, C.Y. Gao, D. Li et al., The extended Q-range small-angle neutron scattering diffractometer at the SNS. J. Appl. Crystallogy **43**, 1068–1077 (2010). https://doi.org/10.1107/S002188981002217X
20. J.D. Beal, K.D. Berry, R.A. Riedel et al., The NOMAD instrument neutron detector array at the SNS. Nucl. Instrum. Meth. A **1018**, 165851 (2021). https://doi.org/10.1016/j.nima.2021.165851
21. J. Ollivier, H. Mutka, L. Didier, The new cold neutron time-of-flight spectrometer IN5. Neutron News **21**, 22–25 (2010). https://doi.org/10.1080/10448631003757573
22. S. Agostinelli, J. Allison, K. Amako et al., Geant4—a simulation toolkit. Nucl. Instrum. Meth. A **506**, 250–303 (2003). https://doi.org/10.1016/S0168-9002(03)01368-8
23. X.G. Wu, Y.B. Zhao, H. Luo et al., Test of a 3He neutron detector readout electronics prototype for CSNS multipurpose physics neutron diffractometer. RDTM **5**, 200–206 (2021). https://doi.org/10.1007/s41605-020-00235-4
24. S. Bönisch, B. Namaschk, F. Wulf, Charge equalizing and error estimation in position sensitive neutron detectors. Nucl. Instrum. Meth. A **570**, 133–139 (2007). https://doi.org/10.1016/j.nima.2006.10.002
25. A. Ravazzani, A.F. Para, R. Jaime et al., Characterisation of 3He proportional counters. Radiat. Meas. **41**, 582–593 (2006). https://doi.org/10.1016/j.radmeas.2005.08.004